

The physical conditions in IRDC clumps from Herschel HIFI observations of H₂O [★]

R.F. Shipman^{1,2}, F.F.S van der Tak^{1,2}, F. Wyrowski³, F. Herpin^{4,5}, and W. Frieswijk⁶

¹ SRON Netherlands Institute for Space Research

² Kapteyn Astronomical Institute, University of Groningen

³ Max-Planck-Institut für Radioastronomie

⁴ Univ. Bordeaux, LAB, UMR 5804, F-33270, Floirac, France

⁵ CNRS, LAB, UMR 5804, F-33270, Floirac, France

⁶ ASTRON Netherlands Institute for Radio Astronomy

ABSTRACT

Context. The earliest phases of high-mass star formation are poorly understood.

Aims. Our goal is to determine the physical conditions and kinematic structure of massive starforming cloud clumps .

Methods. We analyse H₂O 557 GHz line profiles observed with HIFI toward four positions in two infrared-dark cloud clumps . By comparison with ground-based C¹⁷O, N₂H⁺, CH₃OH, and NH₃ line observations, we constrain the volume density and kinetic temperature of the gas and estimate the column density and abundance of H₂O and N₂H⁺.

Results. The observed water lines are complex with emission and absorption components. The absorption is redshifted and consistent with a cold envelope, while the emission is interpreted as resulting from protostellar outflows. The gas density in the clumps is $\sim 10^7$ cm⁻³. The o-H₂O outflow column density is $0.3 - 3.0 \times 10^{14}$ cm⁻². The o-H₂O absorption column density is between 1.5×10^{14} and 2.6×10^{15} cm⁻² with cold o-H₂O abundances between 1.5×10^{-9} and 3.1×10^{-8} .

Conclusions. All clumps have high gas densities ($\sim 10^7$ cm⁻³) and display infalling gas. Three of the four clumps have outflows. The clumps form an evolutionary sequence as probed by H₂O N₂H⁺, NH₃, and CH₃OH. We find that G28-MM is the most evolved, followed by G11-MM and then G28-NH₃. The least evolved clump is G11-NH₃ which shows no signposts of starformation; G11-NH₃ is a high-mass pre-stellar core.

Key words. ISM, Star Formation

1. Introduction

The earliest stages of high-mass star formation are challenging to investigate observationally. Massive stars are rare and typically at large distances and they evolve rapidly during their lifetimes (Mottram et al. 2011) . It is expected that the very beginning of formation is also rapid. In addition, the high extinction and crowded nature of high-mass starforming regions complicate their study. Nevertheless, the formation of high-mass stars is of interest because of their large impact on the Galactic environment (Tan et al. 2014).

Since the late 1990s, the investigation into the very earliest stages has undergone significant growth, in a large part because of the discovery of the so-called infra-red dark clouds (IRDCs) (Beuther et al. 2007). These dark clouds were originally noted in *Infrared Space Observatory* (Perault et al. 1996) and *Midcourse Space eXperiment* (Egan et al. 1998) mid-infrared observations of the Galactic Plane. They are easily seen as isolated dark filamentary patches or silhouettes against the bright Galactic Plane. To be optically thick in the mid IR implies high column densities of gas and dust (10^{22} cm⁻²; Carey et al. 1998). These clouds were not seen in IRAS 100 μ m data, and therefore are likely colder than 20 K (Egan et al. 1998) and at distances of a few to 10 kpc; IRDCs are therefore cold, dense, and massive clouds.

Observations at submm wavelengths (both molecular lines and continuum) not only confirmed the cold, dense, and massive nature of the clouds (Carey et al. 2000; Pillai et al. 2006b,a), but also identified isolated clumps within the IRDC filaments (Johnstone et al. 2003; Rathborne et al. 2006). Further studies reveal that within these clumps are cores in the process of starformation (Ragan et al. 2012; Henning et al. 2010; Beuther et al. 2007, and references therein). The cores often show molecular outflows and/or masers similar to other well-known massive starforming regions. The one main difference is that the forming sources have not yet had time to fully heat up and disrupt their environment (Beuther et al. 2007).¹

Recent investigations have focused on obtaining a chemical inventory within samples of IRDCs (Miettinen 2012; Sanhueza et al. 2012) to try to identify trends and piece together evolution scenarios (Chen et al. 2010). High resolution interferometric observations indicate that the starforming cores are often made up of smaller more compact objects pointing to cluster formation as opposed to the formation of a single star (Rathborne et al. 2009; Zhang et al. 2009; Wang et al. 2011, 2014).

Observations of water transitions in starforming regions with the *Herschel Space Observatory* have opened a new means of probing the processes occurring during star formation. Water exposes many dynamic effects such as outflows, but water absorp-

[★] *Herschel* is an ESA space observatory with science instruments provided by European-led Principal Investigator consortia with important participation of NASA.

¹ This paper uses the term "clump" to identify a part of the IRDC which has an enhancement of either submm or NH₃ emission. For approximate scales, IRDCs: 10 pc, clumps: 0.5 pc, cores: 0.05 pc.

tion also reveals many foreground clouds (Marseille et al. 2010). Water abundances are sensitive to temperature as the water sublimates from grain surfaces (Herpin et al. 2012) and show very complex structures within massive starforming clumps.

The goal of this paper is to present the results of *Herschel*-HIFI and *APEX* observations of a sample of IRDCs clumps at different evolutionary stages and to compare these results with other starforming regions observed by HIFI. This paper presents $\text{o-H}_2\text{O } 1_{10} \rightarrow 1_{01}$ and $\text{C}^{17}\text{O } 3 \rightarrow 2$ observations of four starforming clumps from two different clouds G28.34+0.06 and G11.11-0.12. The active clumps are chosen based on their bright submm continuum (Rathborne et al. 2006) while the quiescent clumps are chosen based on their prominent NH_3 line emission (Pillai et al. 2006a). The sources have been relatively well studied in the literature which allows our observations of the clumps to be placed into an existing context.

Figures 1 and 2 show $850 \mu\text{m}$ images of the two IRDCs². The two clumps in G28.34+0.06 are labelled G28-NH₃ for the position chosen based on NH_3 emission (Pillai et al. 2006a) and G28-MM for the position chosen based on the strongest submm emission (Rathborne et al. 2006). Likewise, two positions in G11.11-0.12 are labelled G11-NH₃ (NH_3 peak, Pillai et al. 2006a) and G11-MM (continuum peak, Rathborne et al. 2006).

Table 1 lists general clump properties. Clump systemic velocity, gas temperature are based on NH_3 observations while clump mass and total column density are based on dust continuum emission (Carey et al. 1998; Pillai et al. 2006b). Kinematic distances to the clumps are taken from Carey et al. (1998) and are based the radial velocity of molecular line emissions and the galactic rotation curve. The positions and Herschel observations are shown in Table 2.

The clumps span a range of evolutionary stages. Both G28-MM and G11-MM stand out as prominent point sources in PACS photometry (Ragan et al. 2012). Both sources are also associated with CH_3OH and/or H_2O maser emission (Pillai et al. 2006b; Wang et al. 2008, 2014) and both are seen to fragment into substructures at high spatial resolution (Zhang et al. 2009; Wang et al. 2014). A CH_3OH outflow is observed for G11-MM (Leurini et al. 2007; Gómez et al. 2011; Wang et al. 2014) and G28-MM was found to harbour a "hot-core" Zhang et al. (2009). These clumps are active.

The clump G28-NH₃ was studied together with G28-MM and found to be of a younger evolutionary stage based on deuteration level (Chen et al. 2010). Neither NH_3 clump is identified in Ragan et al. (2012). Based on their maps, G28-NH₃ and G11-NH₃ are seen at SPIRE wavelengths but do not stand out as point sources at PACS wavelengths implying low temperatures (< 16 K). These clumps are not active.

In Sect. 2 we give details of the observations and data reduction. The line fitting procedure and results are presented in Sect. 3. The column densities of H_2O , N_2H^+ , C^{17}O , and CH_3OH as well as gas densities based on N_2H^+ and CH_3OH transitions are discussed in Sect. 4. In Sect. 5 the various dynamic structures in the clumps are discussed and an evolutionary sequence is proposed and the H_2O results are compared with other starforming regions.

² Data from the SCUBA instrument on The James Clerk Maxwell Telescope are used for this investigation. The JCMT is operated by the Joint Astronomy Centre on behalf of the Science and Technology Facilities Council of the United Kingdom, the Netherlands Organisation for Scientific Research, and the National Research Council of Canada.

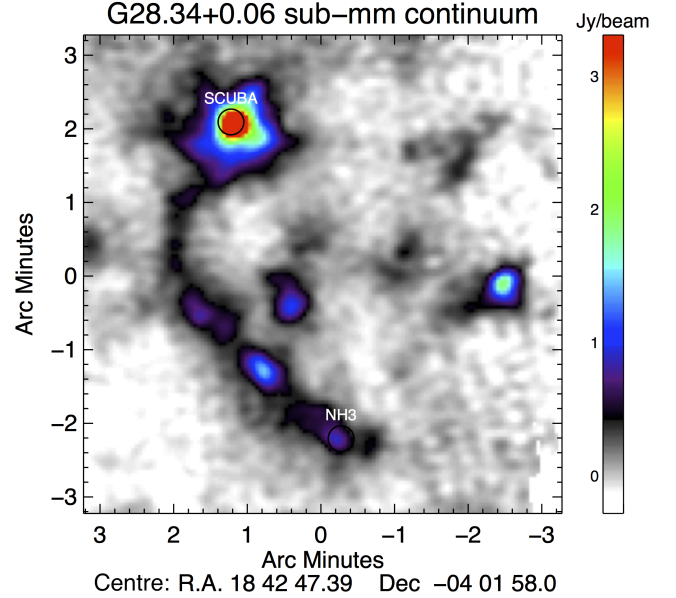


Fig. 1: SCUBA $850 \mu\text{m}$ image of G28.34+0.06. The positions of the observed clumps are labelled as "SCUBA" for the submm position and "NH₃" for the NH_3 position. The image is colour scaled from black (331 mJy/beam) to red (5951 mJy/beam). Every change in colour is roughly an increase of 331 mJy/beam. At a distance of 4.8 kpc, one arcminute is about 2 pc

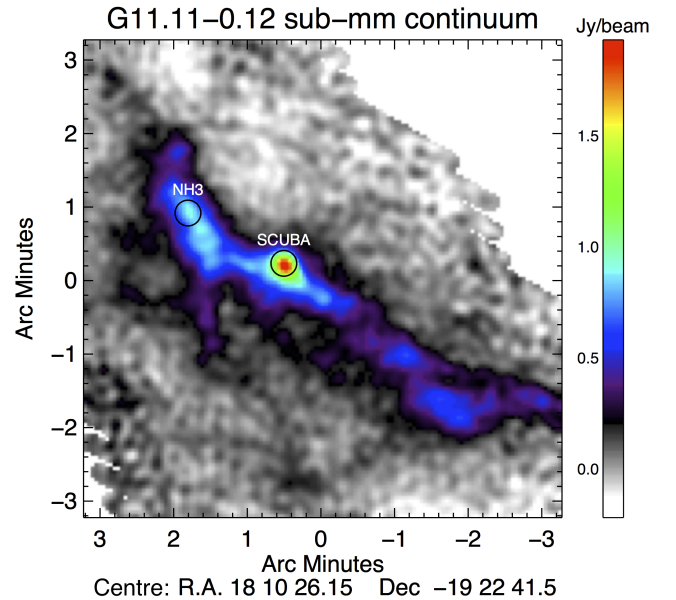


Fig. 2: SCUBA $850 \mu\text{m}$ image of G11.11-0.12. The positions of the observed clumps are labelled as "SCUBA" for the submm position and "NH₃" for the NH_3 position. The image is colour scaled from black (290 mJy/beam) to red (1932 mJy/beam). Every change in colour is roughly an increase of 290 mJy/beam. At the distance of 3.6 kpc, one arcminute is about 1.5 pc.

Table 1: Gas properties of clumps

ID	v_{LSR}^1 (km s^{-1})	T_{kin}^1 (K)	$N(\text{H}+\text{H}_2)^1$ (10^{22} cm^{-2})	Distance ² (kpc)	Mass ¹ (M_{\odot})
G28-NH ₃	80.2	13.2	5.9	4.8	374
G28-MM	78.5	16.0	32.7	4.8	2310
G11-NH ₃	30.4	12.7	8.4	3.6	485
G11-MM	29.2	13.8	10.2	3.6	172

Notes. References. (1) Pillai et al. (2006a); (2) Carey et al. (1998)

2. Observations

2.1. Herschel/HIFI observations

The o-H₂O ground state line observations were carried out as a part of the "Water In starforming regions with Herschel" key programme (WISH, van Dishoeck et al. 2011) with the HIFI instrument (de Graauw et al. 2010) on *Herschel* (Pilbratt et al. 2010).

The observations were made with HIFI Band 1A using the double beam switch observing mode. The sideband separation of 8 GHz and IF bandwidth of 4 GHz allow a local oscillator (LO) setting where the o-H₂O $1_{10}-1_{01}$ transition at 556.9361 GHz, the H₂¹⁸O $1_{10}-1_{01}$ line at 547.676 GHz and the N₂H⁺ 6-5 transition at 558.96 GHz are observed simultaneously. HIFI has two spectrometers, the acousto-optical Wide Band Spectrometer (WBS) and the correlator-based High Resolution Spectrometer (HRS). The data from WBS have a resolution of 1.1 MHz (0.5 km s^{-1} at 557 GHz) and the HRS was configured in two sub-bands centred on the H₂O and H₂¹⁸O lines with a resolution of 0.24 MHz (0.11 km s^{-1}). The N₂H⁺ line was only observed with the WBS.

The observations were started during the Science Demonstration phase of HIFI. In these early observations, spurious signals due to an impure LO signal were still present at frequencies near the 557 GHz water line. The "water spur" affects mainly the very centre of the IF as the observations were set up. In the earliest observations of G11.11-0.12 the spurious responses hampered a proper observation of the N₂H⁺ and H₂¹⁸O lines. These observations were repeated at a later date to improve the signal to noise and take advantage of the purified LO chain. Care was taken to make sure that data used in this study do not contain spurs.

The HIFI data were reduced and further analysis performed using the standard HIPE software³. The HIFI pipeline included updated beam efficiencies as listed in Roelfsema et al. (2012). The vertical and horizontal polarization data have been inspected for standing waves and spurious signals separately. Data from OBSID 134194462 have a low level standing wave which was removed using standard processing. Finally, the double sideband data are corrected to single sideband by estimating and subtracting the emission from the image sideband. This procedure is described in Appendix A. The data shown in Fig. 3 show single sideband data.

For the N₂H⁺ (6 – 5) line in G11.11, only OBSIDs 1342205490 and 1342206660 were used since spurious signals are present in the other observations on these sources. Table 2 lists which line frequencies in which dataset are effected by

³ Pipeline processing, data analysis and line fitting were carried out with the HIPE 10.0 software (Ott 2010) and the CASSIS plugin for HIPE and Cologne Database for Molecular Spectroscopy (Müller et al. 2005, <http://www.astro.uni-koeln/cdms>). CASSIS has been developed by IRAP-UPS/CNRS (<http://cassis.irap.omp.eu>).

spurs. When possible, both polarizations and multiple observations were co-added.

The HRS data were used for the H₂¹⁸O lines and smoothed to 1.1 MHz resolution. HRS data were also used for the H₂O lines for G11-NH₃ and G11-MM. The HRS band was not broad enough for the G28-MM H₂O emission and the H₂O line was placed too close to the edge of the HRS band to use for G28-NH₃. When smoothed, the HRS gives consistent results with the WBS.

2.2. The APEX observations

Complementary observations were carried out between October 2005 and August 2006 with the 12-m Atacama Pathfinder Experiment telescope (APEX, Güsten et al. 2006)⁴ using the APEX-2 345 GHz facility receiver (Risacher et al. 2006). The receiver was tuned to 279.5 (N₂H⁺ 3–2) and 337.8 (C¹⁷O 3–2) GHz. As backend the 2×1 GHz facility FFTS spectrometer (Klein et al. 2006) was used and the observations included the C³⁴S 7–6 and CH₃OH 7_K-6_K lines along with C¹⁷O 3–2. To increase the signal-to-noise the resulting spectra were smoothed to a velocity resolution of 0.87 km s^{-1} . The observations were carried out under excellent weather conditions with PWV of 0.5 mm, leading to DSB system temperatures of about 130 K. The focus was adjusted on Jupiter and the pointing was corrected with continuum cross-scans on the nearby hot core G10.47+0.03. A beam efficiency of 0.73 was applied to convert the data to the T_{mb} scale.

We note that there is a pointing offset up to 22" between the APEX N₂H⁺ (3–2) observations and the HIFI observations. Although APEX observation falls within the 38" HIFI beam the utility is questionable and is kept to provide an indication of the line strength assuming the emission is extended. The offsets are indicated in Table 4.

3. Results

Figure 3 shows the observations of the main lines from Table 3. All four clumps show saturated H₂O absorption and three of the four clumps also have broad emission with self absorption. The clump G11-NH₃ only shows absorption. The H₂¹⁸O line is seen in three sources the exception being G11-MM. The C¹⁷O (3–2), N₂H⁺ (3–2) and N₂H⁺ (6–5) emission lines are detected at all four positions. The N₂H⁺ (3–2) data for G28-MM indicate self absorption. The C¹⁷O (3–2) and N₂H⁺ (6–5) data for G28-NH₃ are marginal detections while the CH₃OH and C³⁴S lines (not

⁴ This publication is based on data acquired with the Atacama Pathfinder Experiment (APEX). APEX is a collaboration between the Max-Planck-Institut für Radioastronomie, the European Southern Observatory, and the Onsala Space Observatory.

Table 2: Overview of observations

Short name	Long Name ^a	OD ^b	OBSID ^c	Spur ^d	RA ^e (J2000)	DEC ^e (J2000)	$\Delta(\text{RA})^f$ (")	$\Delta(\text{Dec})^f$ (")
G28-NH ₃	G28.34+0.06 P3	332	1342194461	N ₂ H ⁺	18 42 46.40	−4 04 12.0	0.007	−0.742
		707	1342219195				−0.051	−0.75
G28-MM	G28.34+0.06 P2	332	1342194462		18 42 52.40	−3 59 54.0	−1.11	−1.01
		694	1342218945				−1.098	−1.00
G11-NH ₃	G11.11-0.12 P1	291	1342191497	N ₂ H ⁺	18 10 33.90	−19 21 48.0	−	−
		496	1342205490				−1.308	−0.682
G11-MM	G11.11-0.12 P2	291	1342191498	N ₂ H ⁺	18 10 28.40	−19 22 29.0	−	−
		520	1342206660				−1.298	−0.702

Notes. ^(a) Name of NH₃ source given in Pillai et al. (2006a). ^(b) Operational day of the Herschel mission ^(c) Herschel identification number ^(d) Spur interferes with the listed transition ^(e) Requested pointing ^(f) Pointing offset (arcsec) based on reconstructed pointing between ODs 320 and 750

Table 3: Observed lines

Species	Frequency ¹ (GHz)	E_u^2 (K)	HPBW (")	Observatory	η_{mb}	T_{sys} (K)	δv (km s ^{−1})
o-H ₂ O 1 ₁₀ → 1 ₀₁	556.93607	61.0	38	HIFI 1A	0.75	76	0.6
o-H ₂ ¹⁸ O 1 ₁₀ → 1 ₀₁	547.67644	60.5	39	HIFI 1A	0.75	76	0.6
N ₂ H ⁺ 6 → 5	558.96666	93.9	38	HIFI 1A	0.75	76	0.6
N ₂ H ⁺ 3 → 2	279.511701	26.8	22	APEX	0.73	120 – 210	0.53
C ¹⁷ O 3 → 2	337.061129	32.4	18	APEX	0.73	130	0.87
C ³⁴ S 7 → 6	337.396459	64.8	18	APEX	0.73	130	0.87
CCH 4 ₅₅ → 3 ₄₄ ^a	349.337706	42.0	18	APEX	0.73	130	0.87
CCH 4 ₄₄ → 3 ₃₃ ^b	349.399276	42.0	18	APEX	0.73	130	0.87
CH ₃ OH 4 ₀ → 3 _{−1} −E	350.687662	28.0	18	APEX	0.73	130	0.87
CH ₃ OH 7 _{−1} → 6 _{−1} −E	338.344588	70.6	18	APEX	0.73	130	0.87
CH ₃ OH 7 ₀₊ → 6 ₀₊ −A	338.408698	65.0	18	APEX	0.73	130	0.87
CH ₃ OH 7 ₀ → 6 ₀ −E	338.124488	78.1	18	APEX	0.73	130	0.87
CH ₃ OH 7 ₁ → 6 ₁ −E	338.614936	86.1	18	APEX	0.73	130	0.87
CH ₃ OH 7 ₂ → 6 ₂ −E	338.721693	87.3	18	APEX	0.73	130	0.87
CH ₃ OH 7 _{−2} → 6 _{−2} −E	338.722898	90.9	18	APEX	0.73	130	0.87
CH ₃ OH 7 _{−2−} → 6 _{−2−} −A	338.512853	102.7	18	APEX	0.73	130	0.87

Notes. References. (1) Müller et al. (CDMS 2005); (2) Schöier et al. (LAMDA 2005) ^(a) Line possibly blended with 4₅₄ – 3₄₃ at 349.338988 GHz ^(b) Line possibly blended with 4₄₃ – 3₃₂ at 349.400671 GHz

shown here) are detected in the submm clumps : G28-MM and G11-MM.

The emission lines are parametrized by fitting single or multiple Gaussians to the data excluding the absorption features. All the H₂O emission lines display complex emission lines which are well represented by two broad Gaussian components. Table 4 lists the results of Gaussian fits to each line.

The procedure used to describe the H₂O and H₂¹⁸O absorption lines is described below.

3.1. Fitting of absorption-emission features

In this work, emission and absorption lines are treated differently. The emission lines are parametrized with single or multiple Gaussian fits. The continuum emission is taken as a first order polynomial. The total emission is the sum of all the components,

$$I_\nu = I_{\nu cont} + \sum_i G_\nu(I_{0,i}, \nu_{0,i}, \Delta\nu_i),$$

where $I_{\nu cont}$ is the single sideband estimate of the continuum and G_ν is the Gaussian parametrized by the intensity I_0 , central frequency ν_0 and width $\Delta\nu_0$ for each emission component. The data used to determine these parameters are at frequencies which do

not show signs of absorption. The emission lines and continuum are shown in Fig. 4. The sum of the resulting Gaussian curves and the continuum then represents the total emission.

To measure the absorption lines, the data are normalized by dividing out the total emission. Normalized data are then fit for a Gaussian absorption component. The total absorption is the product of each absorbing component,

$$I_{\nu, norm} = \prod_i \exp^{-\tau_{\nu i}},$$

where τ_ν is itself a Gaussian absorption feature.

Figure 5 shows the absorption features in relative units, and the results of the fitting procedure are as follows. The clump G28-NH₃ is well fit by a single absorbing component at 81.4 km s^{−1}; G28-MM requires at least two components, one broad component at 79.3 km s^{−1} and another at 82.8 km s^{−1}. The main absorption model for G28-MM is not particularly satisfying. The model underestimates the blue absorption and overestimates the red. It does however, provide a sufficient representation of the width and depth of the main absorption. Multiple components for the main feature are possible but are highly degenerate with regards to depth and width without providing more information. We choose for simplicity to retain only one main absorption feature. The clump G11-NH₃ can be well fit

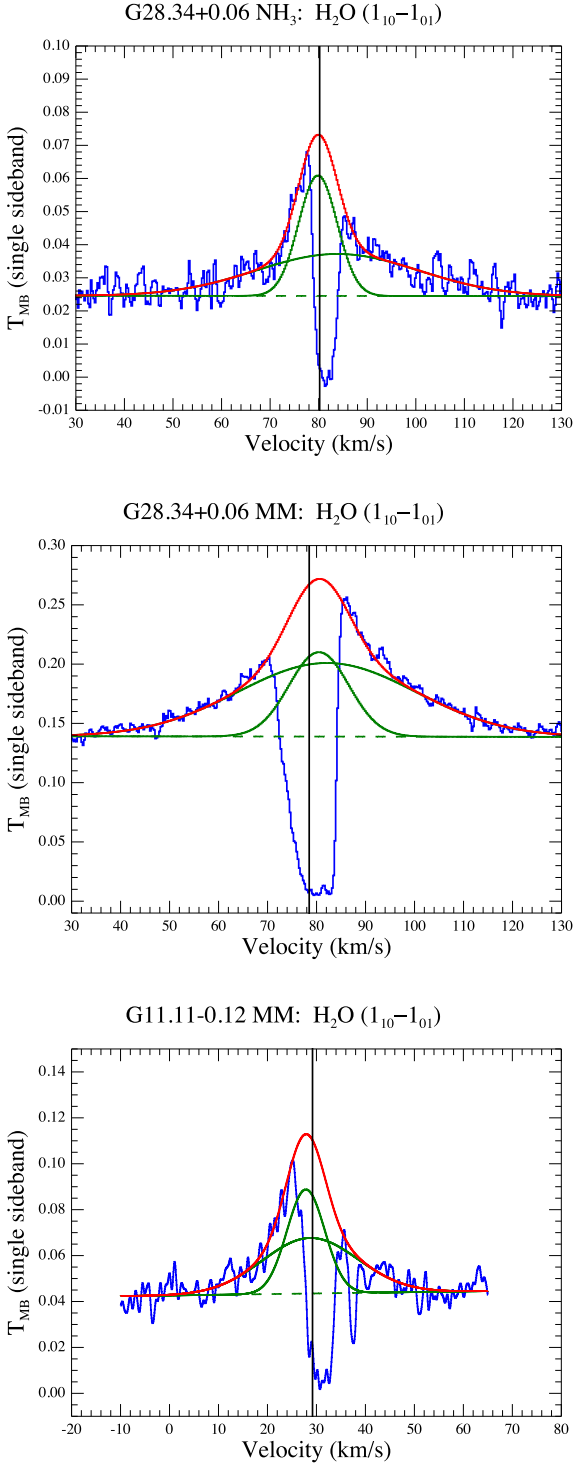


Fig. 4: Water emission seen in three clumps. Emission lines are fit with two Gaussian components (solid green). The continuum is a first order polynomial fit (dashed green). The total emission is the sum of the two components and the continuum (shown in red).

by a broad absorption at 31.2 km s^{-1} , a fully saturating feature at 33.2 km s^{-1} and a narrow feature at 37.1 km s^{-1} . It is notable that the broad absorption is not saturated unlike in the other clumps. The clump G11-MM is reasonably well fit by a broad absorption feature at 30.9 km s^{-1} and a narrow feature at 37.5 km s^{-1} .

4. Analysis

4.1. Line velocities

Inspection of Table 4 reveals three different types of molecular lines. The emission lines all appear at or near the systemic velocity of the clumps. The H_2^{18}O lines are in absorption at the systemic velocity. The H_2O absorption features either appear well offset ($> 5 \text{ km s}^{-1}$) or at the systemic velocity with a redshifted wing. The highly offset lines are presented in Sect. 5.1 while the broad redshifted features will be discussed in more detail in Sect. 5.2.

4.2. Line widths

The widths of the H_2O emission range from 9 km s^{-1} to 43 km s^{-1} . Each clump displaying emission lines is best fit by two lines, a broad (9 to 14 km s^{-1}) and a very broad (23 to 43 km s^{-1}) line. H_2O absorption lines are usually broader than other molecular line transitions for the clumps. When absorption occurs away from the systemic velocity (for example G11-NH₃ and G11-MM absorption near 37 km s^{-1}), the line widths are much narrower (1.5 to 2 km s^{-1}) and similar to the absorption in foreground clouds observed by Flagey et al. (2013). The H_2^{18}O line widths are notably narrow ($< 2 \text{ km s}^{-1}$) and at the systemic velocity.

Transitions of CH_3OH are detected in both G28-MM and G11-MM. In G28-MM, the data quality is sufficient to detect two emission components, one broad and one intermediate for the transitions $\text{CH}_3\text{OH } 4_0 \rightarrow 3_{-1}\text{-E}$, $\text{CH}_3\text{OH } 7_{-1} \rightarrow 6_{-1}\text{-E}$, and $\text{CH}_3\text{OH } 7_{0+} \rightarrow 6_{0+}\text{-A}$. The transitions, $\text{CH}_3\text{OH } 7_2 \rightarrow 6_2\text{-E}$ and $\text{CH}_3\text{OH } 7_{-2} \rightarrow 6_{-2}\text{-E}$ are blended. In this case the central velocity is fixed and both lines are fit simultaneously to give the results in Table 4.

Based on Table 4 it is possible to identify 3 width regimes of lines at the systemic velocity: narrow ($< 3 \text{ km s}^{-1}$), intermediate ($3\text{-}7 \text{ km s}^{-1}$) and broad ($> 7 \text{ km s}^{-1}$). Table 5 places each transition in one of these categories for each clump.

4.3. Column density from emission lines

Table 6 lists the column densities for H_2O , N_2H^+ , C^{17}O , and C^{34}S (if present) for the four clumps. The column densities are estimated using the LAMDA molecular database (Schöier et al. 2005) and the RADEX radiative transfer code (van der Tak et al. 2007) based on the line strengths and widths presented in Table 4. Since only one transition is observed for these species, the kinetic temperature observed for NH_3 (Pillai et al. 2006a) is used for three different gas densities: 10^5 , 10^6 and 10^7 cm^{-3} . It is recognized that the application of a uniform density and temperature cannot truly describe the clumps. The RADEX results, however, can provide indications of abundances for comparison with other published results.

As can be seen in Table 6, the C^{17}O emission lines are insensitive to the gas density. The CO column density provides an alternative measure of the total H_2 column density which has been estimated from dust continuum emission in Pillai et al. (2006a). Taking the canonical C^{17}O abundance as 4.8×10^{-8} (Frerking et al. 1982), we derive an H_2 column density for the four clumps which is 3 to 7 times lower than the one that is obtained based on dust emission. This underabundance is similar to that found for low mass pre-stellar cores and attributed to CO depletion (Bacmann et al. 2002).

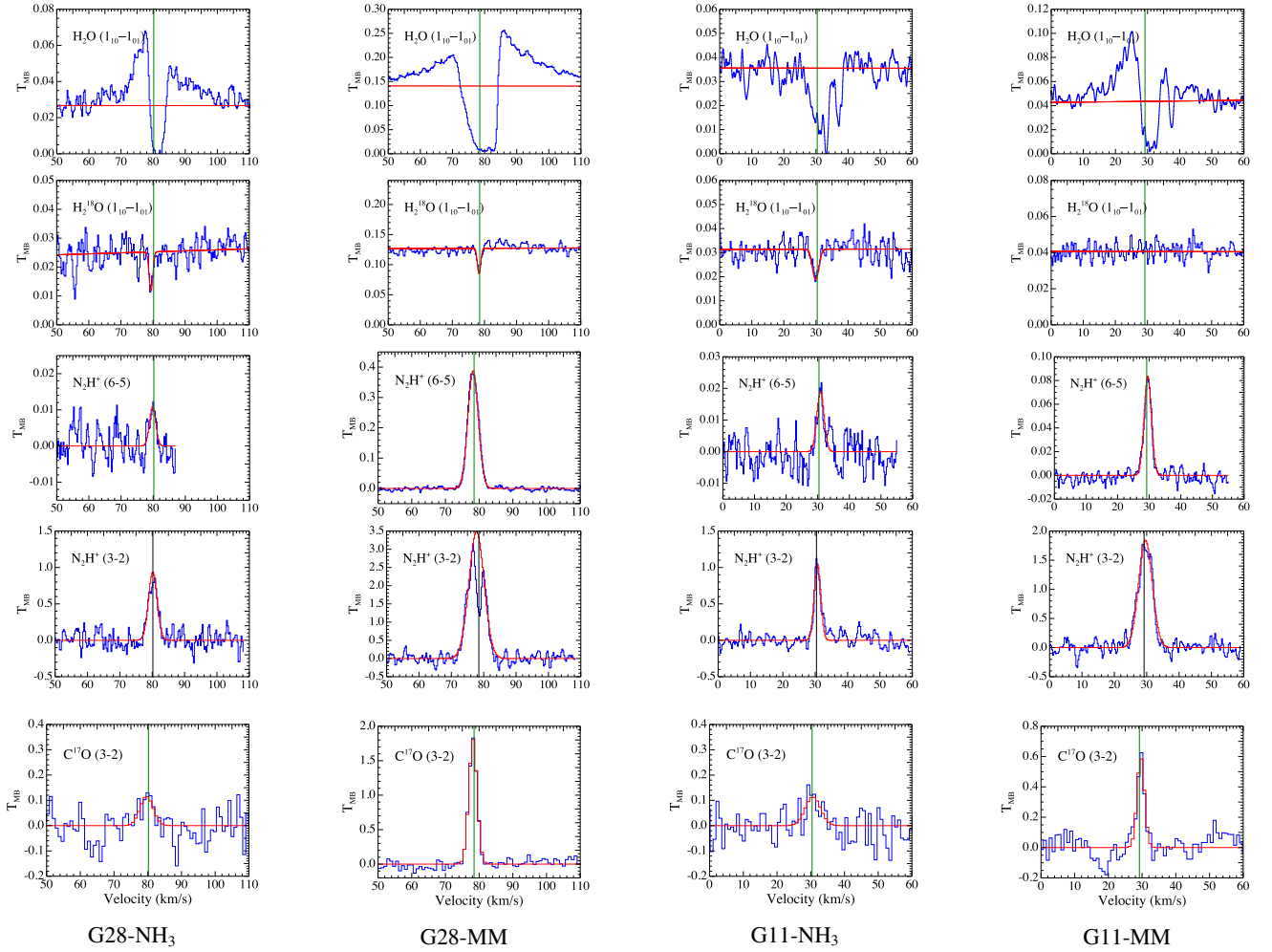


Fig. 3: Data for HIFI and APEX ($C^{17}O$ and N_2H^+) observations for each clump and transition are shown in blue. Gaussian fits are indicated in red except for the water transition where only the continuum level is shown in red. The systemic velocity of each clump is indicated with a green line. The complex profiles of the main H_2O line are clearly visible. The full model decompositions of both emission and absorption are shown in Figs. 4 and 5 respectively.

An estimation of the gas density is possible based on analysis of the two different transitions of N_2H^+ . The RADEX code is used to determine transition line flux ratios (where flux=width \times peak intensity) of N_2H^+ (3-2) to N_2H^+ (6-5) for isothermal, uniform density and optically thin clouds. Figure 6 shows the temperature vs density trends for the N_2H^+ line flux ratios from 10 to 130. At a given gas temperature, the figure can be used to narrow the appropriate range of densities.

The measured flux ratios (and errors) are 110 (26) for G28-NH₃, 13 (1) for G28-MM, 41 (5) for G11-NH₃ and 40 (2) for G11-MM. The temperatures of the clumps determined from NH₃ are from 12.7 K to 16 K. Clump temperatures around 15K would imply densities between $3 \times 10^6 \text{ cm}^{-3}$ to $3 \times 10^7 \text{ cm}^{-3}$. The clumps would have to be significantly warmer ($> 25 \text{ K}$) than what is found for NH₃ to support densities of 10^5 cm^{-3} or lower. The exception to this is G28-MM which has a ratio of only 13, perhaps indicating a warmer interior temperature.

We note that the N_2H^+ (3-2) APEX observation is roughly 20'' off of the G11-NH₃ position. The analysis followed here can only be used to give a general indication of the density of G11-NH₃. If the flux ratio is a factor of two higher, the resulting density would be about 10^6 cm^{-3} .

We have explored the effect of increasing optical depth by increasing the cloud column density in the RADEX calculations by an order of magnitude. An increase in the optical depth will decrease the density by roughly an order of magnitude for a given temperature and line ratio putting the range of densities for the clumps between $3 \times 10^5 \text{ cm}^{-3}$ to $3 \times 10^6 \text{ cm}^{-3}$.

These densities are consistent with earlier published results on N_2H^+ in G28.34+0.06 (Chen et al. 2010) and $C^{34}S$ in G11-MM (Gómez et al. 2011).

4.3.1. The o- H_2O emission

The H_2O line profiles are quite different from those of the other lines. When emission is detected (G28-NH₃, G28-MM, and G11-MM), the line is very broad with line widths of 9 to 45 km s^{-1} . Like for other high mass H_2O proto-stellar cores (e.g. van der Tak et al. 2010), our data are better fit by two broad emission components, a broad component from 9 to 15 km s^{-1} wide and a very broad component 23 km s^{-1} or greater. As in van der Tak et al. (2010) this component is identified as an outflow.

It is difficult to accurately estimate the column density of H_2O in the outflow. The process giving rise to this component is

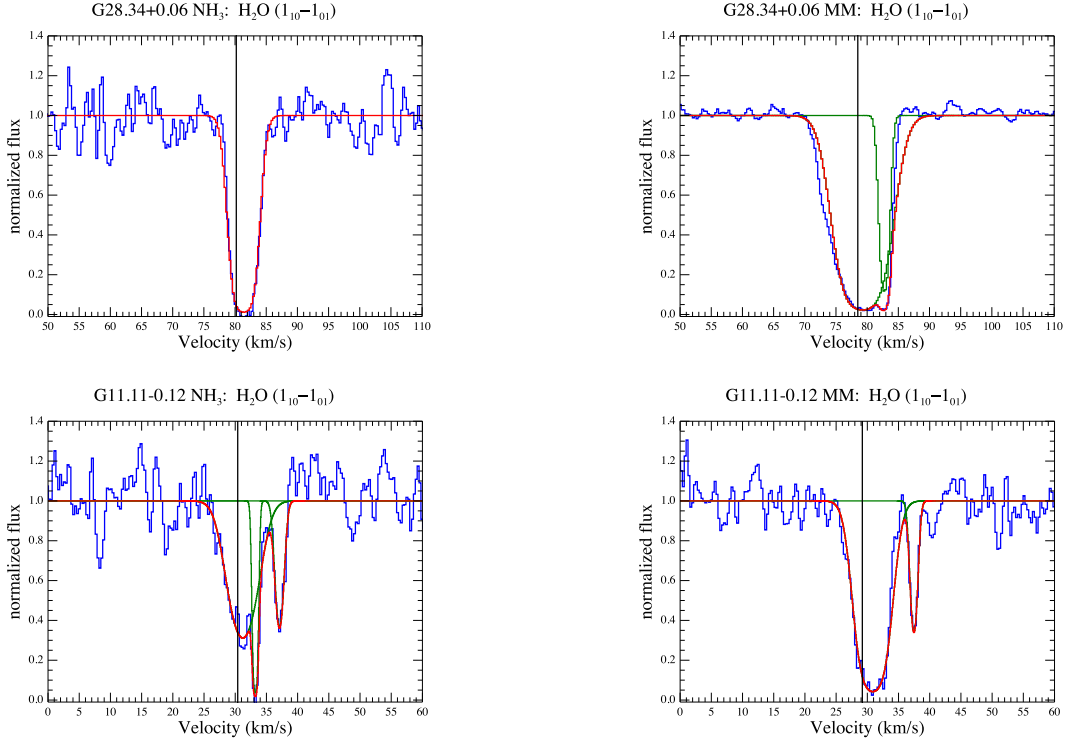


Fig. 5: Main water absorption component in each clump. The data have been normalized by the total emission models (see Sect. 3.1). The individual models are indicated in green whereas total absorption models are shown in red.

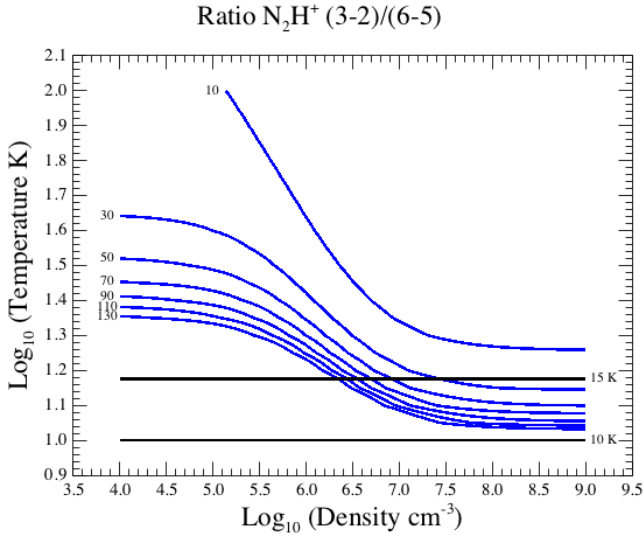


Fig. 6: Temperature/density trends of the N_2H^+ (3-2)/(6-5) flux ratio for uniform density, isothermal and optically thin clouds. Curves of constant flux ratio are shown in blue. The flux ratio value of each contour is listed. The black solid line indicates gas temperatures of 10 K and 15 K which are roughly the ranges of the 4 clumps.

not quiescent and therefore probably at quite different temperatures and densities than the material seen in NH_3 , N_2H^+ or $C^{34}S$.

Table 7: Outflow column density for o- H_2O

Line	Velocity ($km\ s^{-1}$)	Δv ($km\ s^{-1}$)	T_{mb} (mK)	N ($10^{14}\ cm^{-2}$)
G28-NH ₃				
o- H_2O	83.9 (0.7)	39.5 (2.0)	13 (1)	0.5
o- H_2O	79.8 (0.1)	9.3 (0.4)	36 (2)	0.3
G28-MM				
o- H_2O	82.1 (0.2)	42.9 (0.9)	62 (2)	3.0
o- H_2O	80.5 (0.2)	14.4 (0.6)	71 (4)	1.1
G11-MM				
o- H_2O	28.7 (0.2)	23.0 (1.3)	24 (4)	0.6
o- H_2O	27.8 (2.0)	9.1 (2.3)	43 (2)	0.4

Notes. Column density estimate assuming outflow properties of $T_{kin} = 200\ K$ and $n(H_2) = 3 \times 10^4\ cm^{-3}$ from van der Tak et al. (2010).

Even $C^{17}O$ is following the dense core and not tracing the outflow. In light of these difficulties, we follow the approach of van der Tak et al. (2010) and calculate the column density in the outflows assuming that $T_{kin} = 200\ K$ and $n = 3 \times 10^4\ cm^{-3}$. These results are shown in Table 7.

4.4. Column density from o- H_2O absorption

The column density of the absorbing water follows readily from the depth of the line and its width (Plume et al. 2004). Table 8 shows the column density and abundance of water based on absorption measurements. In some cases, the values listed are

lower limits to the column density, since the water absorption lines are close to saturation.

Table 8 also shows the results from H_2^{18}O . The isotope provides an independent measurement of the water column density when present or an upper limit when it is not detected. For the upper limits, the depth of the line is estimated as 1σ of the single sideband continuum with a line width of 2 km s^{-1} . The H_2^{18}O absorption features are narrow ($1\text{--}2 \text{ km s}^{-1}$) and at the systemic velocity while the main H_2O features are mostly saturated, broad ($3\text{--}6 \text{ km s}^{-1}$) and redshifted by $\sim 2 \text{ km s}^{-1}$ (see 5.2). This discrepancy implies that part of the absorption seen in H_2O is a different component that what is probed by H_2^{18}O . The abundance listed in Table 8 is only calculated based on the H_2^{18}O data.

Both clumps of G28.34+0.06 display an H_2O absorption complex between 0 and 30 km s^{-1} LSR. These features are shown in Fig. 10 and discussed in Sect. 5.1 below.

4.5. The CH_3OH -E excitation analysis

In the clumps G28-MM and G11-MM CH_3OH transitions are observed. Using the formalism of Helmich et al. (1994) and Blake et al. (1987), rotation diagrams of the CH_3OH transitions can be calculated. The line strength and permanent dipole parameters are taken from Anderson et al. (1990). The resulting rotation diagrams are shown in Figs. 7 and 8. This analysis assumes optically thin transitions in LTE. We use only the narrower line component of G28-MM. The results indicate a rotation temperature of 10 K to 16 K and a column density of CH_3OH of 4.0 to $2.6 \times 10^{15} \text{ cm}^{-2}$. With only three data points for G11-MM, the column density of E- CH_3OH is poorly constrained.

Leurini et al. (2007) observed 5 IRDC clumps in CH_3OH transitions to probe their density and temperature structure. In general they find that clumps need up to three components: an extended component, a core component and an outflow component. One of their clumps is G11-MM. They conclude that two components are needed to describe the emission: extended and core. The kinematic temperatures they derive are $16\text{--}19 \text{ K}$ (extended) and $38\text{--}54 \text{ K}$ (core) They did not observe the 338 GHz band toward this source. The rotation temperature and column density we find is most in agreement with their extended component. Although G28-MM was not observed by Leurini et al. (2007), the broad CH_3OH lines that are found here would be classified as an outflow component.

In order to estimate the density of the gas from which the CH_3OH lines originate, we perform a similar analysis for ratios of CH_3OH lines as for the ratio of N_2H^+ transitions. Choosing the two brightest CH_3OH transitions $7_{-1}\text{--}6_{-1}$ and $7_0\text{--}6_0$, line ratios of 0.77 for G28-MM and 0.13 for G11-MM are obtained. We calculate a grid of RADEX models for densities from 10^4 cm^{-3} to 10^9 cm^{-3} and gas temperatures from 10 K to 100 K. From Fig. 9 we can see that the ratio of the transitions is relatively insensitive to the gas temperature and that for the observed ratio for G11-MM a density of $3 \times 10^6 \text{ cm}^{-3}$ is suggested. For G28-MM, the ratio is quite high which could be indicating that CH_3OH is originating from a higher temperature component. Nevertheless the analysis is indicating high densities $> 10^7 \text{ cm}^{-3}$.

5. Discussion

5.1. Foreground absorption

Each cloud shows absorption features at velocities 5 km s^{-1} or more different from the systemic velocity of the cloud. These

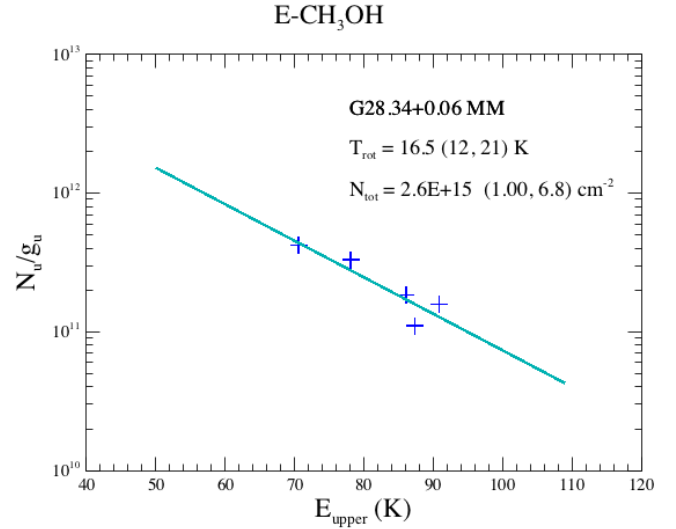


Fig. 7: The E-methanol rotation diagram for G28-MM.

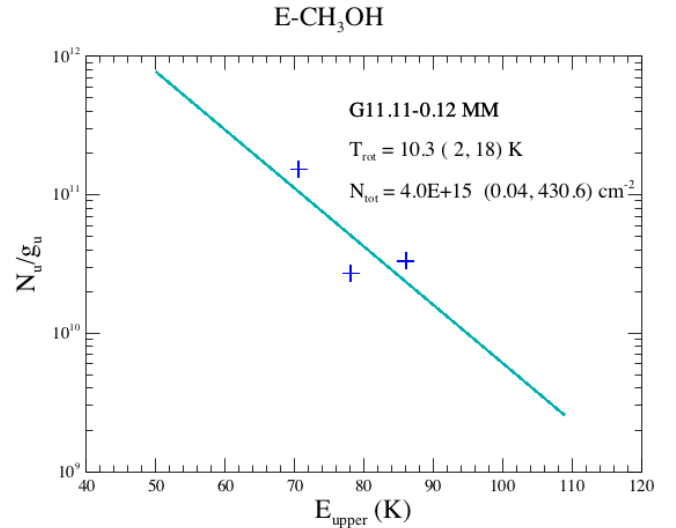


Fig. 8: The E-methanol rotation diagram for G11-MM.

features are usually narrow and not fully saturated. Examples of such clouds are found in Marseille et al. (2010) and Flagey et al. (2013). These are taken to be foreground clouds.

Toward G28-NH₃ and G28-MM there is a complex of water absorption features between 0 and 30 km s^{-1} LSR (see Fig. 10). Column densities for these clouds are estimated to be between $1 \times 10^{12} \text{ cm}^{-2}$ and $4 \times 10^{13} \text{ cm}^{-2}$. Both absorption complexes show roughly similar features (deep narrow absorption around 7 to 9 km s^{-1} , another set around 15 km s^{-1} and again near 22 km s^{-1}). These similar features suggest a common cloud in front of the two clumps with possibly a velocity gradient of a few km s^{-1} between the two clump positions.

In both clumps G11-NH₃ and G11-MM there are features near 37 km s^{-1} . The difference in velocity from systemic as well as the similar width and column densities of the features, suggests that they also originate from foreground clouds. Table 9 lists the velocities, widths and column densities for all features identified as foreground for o-H₂O. The widths and column den-

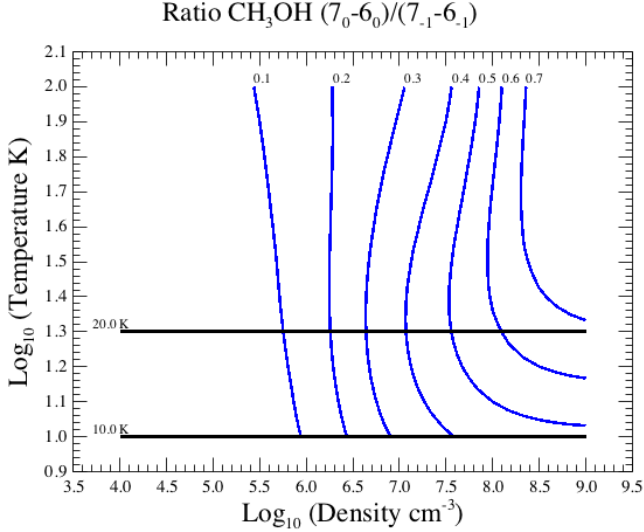


Fig. 9: The CH₃OH-E ratio plot for densities from 10⁴ cm⁻³ to 10⁹ cm⁻³ and gas temperatures from 10 K to 100 K. Curves of constant flux ratio are shown in blue. The flux ratio value is listed above these curves. The black solid line indicates gas temperatures of 10 K and 20 K which are roughly the kinematic temperatures of the rotation analysis.

Table 9: Foreground o-H₂O absorption.

ID	v (km s ⁻¹)	Δv (km s ⁻¹)	τ	N(H ₂ O) (10 ¹⁴ cm ⁻²)
G28-NH ₃	1.4	1.6	0.67	0.05
	7.0	0.9	1.91	0.09
	9.1	0.9	0.45	0.02
	12.5	1.6	0.43	0.03
	14.1	0.7	0.62	0.02
	16.0	1.4	0.87	0.06
	17.7	1.4	0.91	0.06
	20.4	1.2	0.52	0.03
	23.6	1.3	1.30	0.08
	26.3	2.0	0.41	0.04
G28-MM	1.2	2.5	0.24	0.03
	4.3	1.8	0.62	0.05
	8.0	0.8	1.44	0.06
	9.0	0.9	1.04	0.05
	10.4	7.3	1.15	0.41
	17.0	3.4	0.98	0.16
	21.4	2.4	0.75	0.10
25.0	3.5	0.16	0.03	
G11-NH ₃	37.1	1.5	1.0	0.07
G11-MM	37.5	1.2	1.1	0.07

Notes. Table of column density estimates of absorption features at significantly different velocities than the clumps. Features are shown in Fig. 10

sities are very similar to the foreground clouds towards W51 (Flagey et al. 2013).

5.2. Infall

The H₂O absorption is systematically redshifted relative to the systemic velocity of each clump. Since this absorption is seen against the dust continuum emission or the very broad H₂O

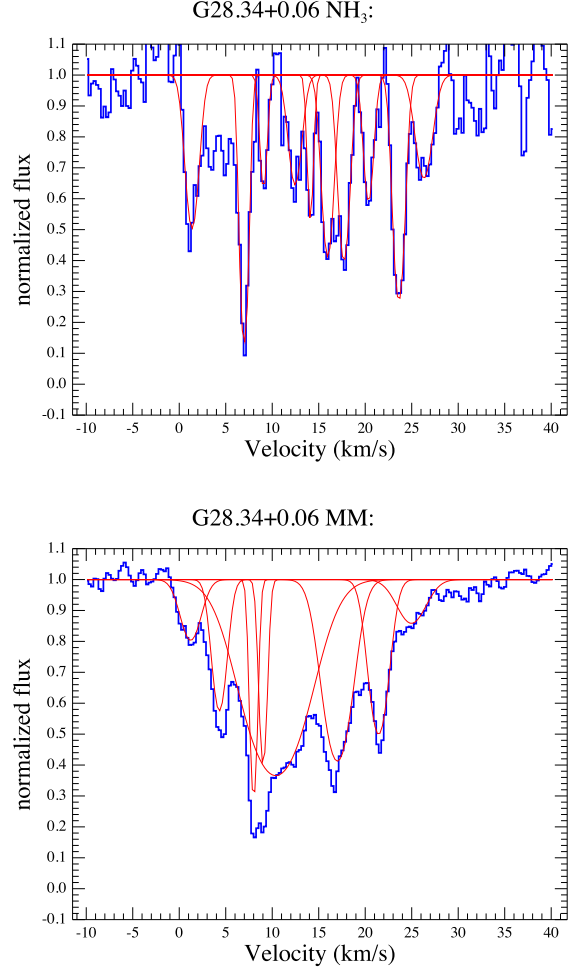


Fig. 10: Absorption for G28-NH₃ and G28-MM between 0 and 30 km s⁻¹ LSR. The data in blue are normalized single sideband flux. Identified features are shown in red.

emission, this motion is detected between the observer and the source of the emission. The absorbing water is moving towards the IRDC clumps. The redshifted absorption is not seen in the H₂¹⁸O absorption lines nor in the N₂H⁺, C¹⁷O, or CH₃OH emission. The completely saturated absorption indicates that the infall is occurring on spatial scales at least as large as the extent of the continuum emission.

If interpreted as gas falling toward a central point, we can attempt to estimate the infalling material rate (Beltrán et al. 2006). The rate is simply the velocity of gas, V_{infall} , at a given distance from the centre, R , the density of this gas, $n(R)$ and the molecular weight μ .

$$\dot{M} = 4\pi R^2 \mu_{H_2} n(R) V_{infall},$$

assuming that the material is falling from every direction toward the centre of the clump and gives an upper limit to the rate if the infall is not uniform. Three of the four clumps have been observed at high spatial resolution. G28-NH₃ and G28-MM in N₂H⁺ (3-2) and continuum (Chen et al. 2010) and G11-MM in CH₃OH and C³⁴S (Gómez et al. 2011). None of the high resolution observations identify infalling gas. The H₂¹⁸O lines are not redshifted and are therefore more associated with the C³⁴S, N₂H⁺ gas. This indicates, therefore, that infalling gas is occurring at larger radii than these observations.

We can then use the sizes determined by the high angular resolution observations to provide an upper limit to the infall rate. Table 10 lists these values under the assumption of three different densities. If the clumps have a power law density structure with an index of -2 , the infall rate should be roughly constant. If this is the case and given the gas density determined by the N_2H^+ and CH_3OH ratios is estimated to be on the order of 10^6 cm^{-3} , our best estimate of the infall rate is $\sim 10^{-3} M_\odot \text{ yr}^{-1}$.

Power laws with index from -1 to -2.5 have been seen observationally and depend on distance from the central source (van der Tak et al. 2000; Beuther et al. 2002). The adoption of a power law of -2 would significantly over estimate the infall rate at large distances and underestimate the rate at close distances. Clearly a physical structure for the clumps model is needed.

5.3. Structure of IRDC clumps

Our observations reveal different dynamical structures. The very broad water lines are readily attributed to molecular outflows. These are a relatively common feature in H_2O observations of starforming regions (van der Tak et al. 2013; Kristensen et al. 2012). Outflows are seen toward three of the four clumps. A further inspection of the CH_3OH data for G28-MM reveals that here too is an outflow in CH_3OH .

In our sample, intermediate line widths ($3\text{-}7 \text{ km s}^{-1}$) are observed in the more complex molecules. This component is most akin to the envelope reported by van der Tak et al. (2013) and possibly the extended component noted by Leurini et al. (2007). We will call this the envelope.

The narrow emission lines of C^{17}O and N_2H^+ and H_2^{18}O absorption are consistent with a more quiescent component most akin to the IRDC filament itself (Pillai et al. 2006a; Henshaw et al. 2013). We will call this the quiescent outer envelope. It is the stage between the gas and dust swept up into the forming proto-star and the molecular cloud filament (IRDC)

Table 11 lays out the various clump components, the properties which distinguish them and the tracers that were used to identify each component.

The H_2O absorption features have intermediate widths, but in all of the clumps in our sample the H_2O is redshifted and the absorption is close to completely saturated. It is not obvious where this layer is to be placed relative to the filament and envelope components. There are three possibilities for where this collapsing absorption layer is occurring.

- Since the line width of the collapsing H_2O is similar to the line width of the more complex molecules like CH_3OH , perhaps the layer is interior to the “envelope” region. This would be a warm and dense infalling gas. It is difficult to imagine that the absorbing layer spatially covers the entire emitting region to produce saturated absorption lines.
- Alternatively, the layer could be between the quiescent outer envelope and the envelope. In this scenario, the central part of the quiescent outer envelope breaks off to fall onto the envelope. Mottram et al. (2013) observed infall from the material surrounding the envelopes of low-mass class 0/I objects. This layer would be intermediate in density between the quiescent outer envelope and the envelope. redshifted wings of other dense tracers like NH_3 , C^{17}O , and N_2H^+ are not seen. Detailed modelling is needed to assess whether this scenario could reproduce the broad saturated lines.
- A final possibility is that the absorbing layer is due to gas falling onto the quiescent outer envelope from the filament itself. In this scenario, the infalling material is essentially

falling onto the clump. Infalling molecular gas onto filaments has been observed onto the DR21 ridge (Schneider et al. 2010). Since IRDCs are also largely filamentary in nature, it should not be surprising to observe infalling material on IRDC clumps. Presumably, the entire IRDC complex would have shown infalling H_2O had it been observed. Since the outer layers of the envelopes have significantly lower line widths than the infalling H_2O , the infalling gas should be relatively low density not to disturb the envelope. This scenario puts the absorbing layer the farthest from the core and dust emission, making it easier to produce saturated absorption. This possibility also provides a natural explanation for the lack of outflow in G11- NH_3 . The collapsing gas seen through the H_2O absorption is not directly linked with the outflow.

5.4. Water in IRDCs

The IRDCs share many similarities with both low mass and high mass proto-stellar objects. The broad H_2O emission in IRDCs is consistent with observations of high mass and low mass proto-stellar objects (van der Tak et al. 2013; Kristensen et al. 2012). Unfortunately without a molecular tracer of the outflowing gas, it is not possible to estimate the abundance of H_2O in the outflow. Further ^{12}CO observations should provide the necessary information to pin down the abundance within the outflow.

The o- H_2O absorption features found here are broader than the low mass counterparts (Kristensen et al. 2012; Mottram et al. 2013) but comparable to the intermediate width features seen in high-mass proto-stellar objects (van der Tak et al. 2013). The narrow features of H_2^{18}O and N_2H^+ are reminiscent of similar features seen towards low mass envelopes.

The fact that H_2^{18}O is not redshifted indicates that there is a quiescent component in the envelope that is not yet participating in any accretion. In another high mass proto-star, W43-MM1, the centres of the H_2^{18}O lines are well aligned with the systemic velocity of the clouds but significantly broader than in this work, while the main isotope lines are redshifted in absorption (Herpin et al. 2012). The source W43-MM1 also shows H_2O absorption on top of broad emission.

In Table 8, we estimated the abundance of water vapour. This calculation assumes that all the H_2 column density as obtained by the dust emission is involved in the collapse. The envelope and core components indicate that parts of clump that are not collapsing. Only a fraction of the H_2 column density is involved in the collapse, which makes our estimate of the water vapour abundance a lower limit. To obtain a better estimate of the abundance, observations of an independent tracer of the collapsing material (e.g. from ^{12}CO or ^{13}CO) are needed.

The water abundance determined from the absorption is consistent with the abundance determined from the low mass source L1544 (Caselli et al. 2012). This level is more indicative of cosmic-ray desorption from grain mantles than thermal evaporation from hot dust. In low mass objects this absorption occurs in a surrounding envelope, either infalling or expanding. The clumps in this work generally only display redshifted infalling motions.

Of the four clumps, G11- NH_3 stands out the most in terms of the lack of molecular complexity and outflow activity. In a recent study of IRDC G11.11-0.12, Henning et al. (2010) detected 24 far-infrared ($70\text{-}140 \mu\text{m}$) sources and were able to further constrain the emission properties of G11-MM. In their work, a source near G11- NH_3 is identified, but close inspection places their source no. 8 more than $20''$ distant from G11- NH_3

(Chavarría 2014); G11-NH₃ has no far-infrared counterpart and is therefore a high-mass pre-stellar core.

6. Conclusions

The main findings in this study are:

- For IRDC clumps, H₂O absorption indicates a low gas phase abundance and is more consistent with desorption of H₂O from dust grains than by heating, similar to low-mass pre-stellar cores.
- Measurements of H₂O together with other molecules provide a picture of the structure of massive clumps on the scale of about 1 pc, from outflow, to envelope and quiescent outer envelope, to infalling gas.
- Analysis of N₂H⁺ and CH₃OH line ratios favour a high internal density ($\sim 10^7$ cm⁻³). Further detailed modelling of each clump will be necessary to determine a proper structure model.
- Molecular clumps within IRDCs are actively forming stars or star clusters, but at different evolutionary stages. NH₃ observations help to identify the earliest stages, but H₂O reveals the infall and outflow dynamics within the clump. Strong far-infrared and CH₃OH emission as well as chemical complexity are signposts for a starforming clump in a later stage of evolution.
- Even with significant infall motions, G11-NH₃ does not display outflow motions nor chemical complexity which are signposts of starformation. This clump appears to be the only starless massive core in our sample.

Based on a detailed analysis of outflow and molecular complexity it is possible to place the clumps in a evolutionary sequence.

1. The clump G28-MM appears to be the most advanced: it is a bright far-infrared source displaying molecular complexity ("hot core"), H₂O and CH₃OH masers, outflows in both H₂O and CH₃OH lines.
2. The clump G11-MM is also an evolved proto-star, also an identified far-infrared source with CH₃OH masers and outflows in H₂O and CH₃OH.
3. The clump G28-NH₃ is not as chemically complex as the submm positions and is not a notable far-infrared source but does display an outflow.
4. The clump G11-NH₃ is the least evolved. It is also not identified in the far-infrared and it does not show outflowing gas, complex molecules nor maser emission.

Acknowledgements. We would like to thank L. Pagani, J. Mottram and E. van Dishoeck for careful readings of this manuscript. We also thank an anonymous referee for thoughtful comments and useful suggestions which significantly improved the final manuscript. HIFI has been designed and built by a consortium of institutes and university departments from across Europe, Canada and the United States under the leadership of SRON Netherlands Institute for Space Research, Groningen, The Netherlands and with major contributions from Germany, France and the US. Consortium members are: Canada: CSA, UWaterloo; France: CESR, LAB, LERMA, IRAM; Germany: KOSMA, MPIfR, MPS; Ireland, NUI Maynooth; Italy: ASI, IFSI-INAF, Osservatorio Astrofisico di Arcetri-INAF; Netherlands: SRON, TUD; Poland: CAMK, CBK; Spain: Observatorio Astronómico Nacional (IGN), Centro de Astrobiología (CSIC-INTA). Sweden: Chalmers University of Technology - MC2, RSS & GARD; Onsala Space Observatory; Swedish National Space Board, Stockholm University - Stockholm Observatory; Switzerland: ETH Zurich, FHNW; USA: Caltech, JPL, NHSC.

References

- Anderson, T., De Lucia, F., & Herbst, E. 1990, *ApJS*, 72, 797
- Bacmann, A., Lefloch, B., Ceccarelli, C., et al. 2002, *A&A*, 389, L6
- Beltrán, M. T., Cesaroni, R., Codella, C., et al. 2006, *Nature*, 443, 427
- Beuther, H., Churchwell, E. B., McKee, C. F., & Tan, J. C. 2007, *Protostars and Planets V*, 165
- Beuther, H., Schilke, P., Menten, K. M., et al. 2002, *ApJ*, 566, 945
- Blake, G. A., Sutton, E. C., Masson, C. R., & Phillips, T. G. 1987, *ApJ*, 315, 621
- Carey, S. J., Clark, F. O., Egan, M. P., et al. 1998, *ApJ*, 508, 721
- Carey, S. J., Feldman, P. A., Redman, R. O., et al. 2000, *ApJ*, 543, L157
- Caselli, P., Keto, E., Bergin, E. A., et al. 2012, *ApJ*, 759, L37
- Chavarría, L. 2014, private communication
- Chen, H.-R., Liu, S.-Y., Su, Y.-N., & Zhang, Q. 2010, *ApJ*, 713, L50
- de Graauw, T., Helmich, F. P., Phillips, T. G., et al. 2010, *A&A*, 518, L6
- Egan, M. P., Shipman, R. F., Price, S. D., et al. 1998, *ApJ*, 494, L199
- Flagey, N., Goldsmith, P. F., Lis, D. C., et al. 2013, *ApJ*, 762, 11
- Ferking, M. A., Langer, W. D., & Wilson, R. W. 1982, *ApJ*, 262, 590
- Gómez, L., Wyrowski, F., Pillai, T., Leurini, S., & Menten, K. M. 2011, *A&A*, 529, A161
- Güsten, R., Nyman, L. Å., Schilke, P., et al. 2006, *A&A*, 454, L13
- Helmich, F. P., Jansen, D. J., de Graauw, T., Groesbeck, T. D., & van Dishoeck, E. F. 1994, *A&A*, 283, 626
- Henning, T., Linz, H., Krause, O., et al. 2010, *A&A*, 518, L95
- Henshaw, J. D., Caselli, P., Fontani, F., et al. 2013, *MNRAS*, 428, 3425
- Herpin, F., Chavarría, L., van der Tak, F., et al. 2012, *A&A*, 542, A76
- Johnstone, D., Fiege, J. D., Redman, R. O., Feldman, P. A., & Carey, S. J. 2003, *ApJ*, 588, L37
- Klein, B., Philipp, S. D., Krämer, I., et al. 2006, *A&A*, 454, L29
- Kristensen, L. E., van Dishoeck, E. F., Bergin, E. A., et al. 2012, *A&A*, 542, A8
- Leurini, S., Schilke, P., Wyrowski, F., & Menten, K. M. 2007, *A&A*, 466, 215
- Marseille, M. G., van der Tak, F. F. S., Herpin, F., et al. 2010, *A&A*, 521, L32
- Miettinen, O. 2012, *A&A*, 540, A104
- Mottram, J. C., Hoare, M. G., Davies, B., et al. 2011, *ApJ*, 730, L33
- Mottram, J. C., van Dishoeck, E. F., Schmalzl, M., et al. 2013, *A&A*, 558, A126
- Müller, H. S. P., Schlöder, F., Stutzki, J., & Winnewisser, G. 2005, *Journal of Molecular Structure*, 742, 215
- Ossenkopf, V. & Henning, T. 1994, *A&A*, 291, 943
- Ott, S. 2010, in *Astronomical Society of the Pacific Conference Series*, Vol. 434, *Astronomical Data Analysis Software and Systems XIX*, ed. Y. Mizumoto, K.-I. Morita, & M. Ohishi, 139
- Perault, M., Omont, A., Simon, G., et al. 1996, *A&A*, 315, L165
- Pillbratt, G. L., Riedinger, J. R., Passvogel, T., et al. 2010, *A&A*, 518, L1
- Pillai, T., Wyrowski, F., Carey, S. J., & Menten, K. M. 2006a, *A&A*, 450, 569
- Pillai, T., Wyrowski, F., Menten, K. M., & Krügel, E. 2006b, *A&A*, 447, 929
- Plume, R., Kaufman, M. J., Neufeld, D. A., et al. 2004, *ApJ*, 605, 247
- Ragan, S., Henning, T., Krause, O., et al. 2012, *A&A*, 547, A49
- Rathborne, J. M., Jackson, J. M., & Simon, R. 2006, *ApJ*, 641, 389
- Rathborne, J. M., Jackson, J. M., Simon, R., & Zhang, Q. 2009, *Ap&SS*, 324, 155
- Risacher, C., Vassilev, V., Monje, R., et al. 2006, *A&A*, 454, L17
- Roelfsema, P. R., Helmich, F. P., Teyssier, D., et al. 2012, *A&A*, 537, A17
- Sanhueza, P., Jackson, J. M., Foster, J. B., et al. 2012, *ApJ*, 756, 60
- Schneider, N., Csengeri, T., Bontemps, S., et al. 2010, *A&A*, 520, A49
- Schöier, F. L., van der Tak, F. F. S., van Dishoeck, E. F., & Black, J. H. 2005, *A&A*, 432, 369
- Tan, J. C., Beltran, M. T., Caselli, P., et al. 2014, *ArXiv e-prints*
- Teyssier, D. & Higgins, R. 2013, *Side-Band Ratio Correction for HIFI Data*, Tech. Rep. Version 1 21/05/2013, Herschel Science Centre
- van der Tak, F. F. S., Black, J. H., Schöier, F. L., Jansen, D. J., & van Dishoeck, E. F. 2007, *A&A*, 468, 627
- van der Tak, F. F. S., Chavarría, L., Herpin, F., et al. 2013, *A&A*, 554, A83
- van der Tak, F. F. S., Marseille, M. G., Herpin, F., et al. 2010, *A&A*, 518, L107
- van der Tak, F. F. S., van Dishoeck, E. F., Evans, II, N. J., & Blake, G. A. 2000, *ApJ*, 537, 283
- van Dishoeck, E. F., Kristensen, L. E., Benz, A. O., et al. 2011, *PASP*, 123, 138
- Wang, K., Zhang, Q., Testi, L., et al. 2014, *MNRAS*, 439, 3275
- Wang, K., Zhang, Q., Wu, Y., & Zhang, H. 2011, *ApJ*, 735, 64
- Wang, Y., Zhang, Q., Pillai, T., Wyrowski, F., & Wu, Y. 2008, *ApJ*, 672, L33
- Zhang, Q., Wang, Y., Pillai, T., & Rathborne, J. 2009, *ApJ*, 696, 268

Appendix A: Sideband calibration

Since the data show both emission and deep absorption, special care must be taken to handle the double sideband nature of the HIFI data. The term "source" sideband refers to the sideband

which contains the frequency of the transition of interest. The "image" sideband refers to the other sideband which is combined in the receiver and ends up in the intermediate frequency. Line absorption occurs against dust and line emission in the source sideband. The double sideband receiver therefore adds line free emission from the image sideband. To correctly calibrate the flux in the source sideband, the continuum flux from the image sideband must be removed. The continuum emission is due to the dust emission and can differ by a few percent between the source and image sidebands which are separated by about 12 GHz. Furthermore, the HIFI mixers in band 1A, are slightly imbalanced also by about a few percent. In the case of the 557 line in band 1A, all the differences between sidebands can result in about a 5% error.

Assuming there is no line emission from the image sideband, a separation of source and image sidebands is possible using the latest sideband ratio determination for the 557 line in band 1A (Teyssier & Higgins 2013) and an estimate of the ratio of the dust emission emissivity between the source and image sidebands. For the later, we used the dust grain models of Ossenkopf & Henning (1994) with thick mantles at 10^6 cm^{-3} . This is the same grain model and dust temperatures used by Pillai et al. (2006b) to determine the dust mass.

The formalism of Flagey et al. (2013) is used to correct for the continuum emission from the image sideband. Each sideband receives a fraction of the emission determined by the sideband gain γ_{upper} or γ_{lower} . The total continuum is then,

$$I_{cont} = \gamma_u I_{u,dust} + \gamma_l I_{l,dust},$$

where,

$$\gamma_u + \gamma_l = 1.0,$$

for normalized gains.

Since a dust model and temperature are assumed, the relative contributions from the dust emission is known and a pseudo continuum from the image sideband can be removed. This was done for the H₂O and H₂¹⁸O data shown in Fig. 3. These figures show the resulting single sideband data.

Table 4: Results of Gaussian line fits

Line	Velocity (km s ⁻¹)	Δv (km s ⁻¹)	T_{mb} or τ^d (mK)	Continuum (mK)	Noise ^e (mK)	notes
G28-NH ₃						
o-H ₂ O 1 ₁₀ → 1 ₀₁	83.9 (0.7)	39.5 (2.0)	13 (1)		3	
o-H ₂ O 1 ₁₀ → 1 ₀₁	79.8 (0.1)	9.3 (0.4)	36 (2)		3	
o-H ₂ O 1 ₁₀ → 1 ₀₁	81.4 (0.1)	3.3 (0.1)	>-4.45	25 (0.5)	3	abs
o-H ₂ ¹⁸ O 1 ₁₀ → 1 ₀₁	79.4 (0.1)	1.2 (0.3)	-0.76 (0.15)	25 (0.5)	9	abs
N ₂ H ⁺ 6 → 5	79.8 (0.2)	2.3 (0.5)	11 (2)		10	^b
N ₂ H ⁺ 3 → 2	80.3 (0.1)	3.4 (0.3)	827 (68)		250	12.5'' ^g
C ¹⁷ O 3 → 2	79.3 (0.8)	5.2 (1.9)	110 (40)		60	^b
C ³⁴ S 7 → 6		60	^a
CH ₃ OH (all lines)		60	^a
G28-MM						
o-H ₂ O 1 ₁₀ → 1 ₀₁	80.5 (0.2)	14.4 (0.6)	71 (4)		4	
o-H ₂ O 1 ₁₀ → 1 ₀₁	82.1 (0.2)	42.9 (0.9)	62 (2)		4	
o-H ₂ O 1 ₁₀ → 1 ₀₁	79.3 (0.1)	6.6 (0.2)	>-3.79	138 (0.5)	4	abs
o-H ₂ O 1 ₁₀ → 1 ₀₁	82.8 (0.1)	1.5 (0.2)	-2.16 (0.02)	138 (0.5)	4	abs
o-H ₂ ¹⁸ O 1 ₁₀ → 1 ₀₁	78.3 (0.1)	1.1 (0.1)	-0.41 (0.03)	129 (0.5)	9	abs
N ₂ H ⁺ 6 → 5	78.2 (0.1)	3.8 (0.1)	404 (2)		5	
N ₂ H ⁺ 3 → 2	77.8 (0.1)	5.45 (0.1)	3580 (140)		240	6.3'' ^g
C ¹⁷ O 3 → 2	78.2 (0.1)	2.9 (0.1)	1800 (40)		60	
C ³⁴ S 7 → 6	77.6 (0.1)	5.6 (0.2)	260 (10)		60	
CCH 4 ₅₅ → 3 ₄₄	78.5 ^c	4.20 (0.07)	680 (10)		60	
CCH 4 ₄₄ → 3 ₃₃	78.5 ^c	4.80 (0.09)	510 (10)		60	
CH ₃ OH 4 ₀ → 3 ₋₁ -E	78.62 (0.06)	4.59 (0.19)	466 (22)		60	
CH ₃ OH 4 ₀ → 3 ₋₁ -E	75.57 (0.42)	10.27 (0.48)	186 (18)		60	
CH ₃ OH 7 ₋₁ → 6 ₋₁ -E	78.35 (0.02)	3.49 (0.07)	1237 (37)		60	
CH ₃ OH 7 ₋₁ → 6 ₋₁ -E	78.02 (0.05)	8.32 (0.22)	702 (38)		60	
CH ₃ OH 7 ₀₊ → 6 ₀₊ -A	78.32 (0.02)	4.38 (0.05)	1917 (23)		60	
CH ₃ OH 7 ₀₊ → 6 ₀₊ -A	77.74 (0.01)	12.12 (0.48)	313 (23)		60	
CH ₃ OH 7 ₀ → 6 ₀ -E	78.23 (0.01)	3.79 (0.03)	880 (6)		60	
CH ₃ OH 7 ₀ → 6 ₀ -E	78.23 (0.01)	3.79 (0.03)	880 (6)		60	
CH ₃ OH 7 ₁ → 6 ₁ -E	78.62 (0.02)	3.90 (0.04)	492 (5)		60	
CH ₃ OH 7 ₂ → 6 ₂ -E	78.5 ^h	4.02 (0.17)	261 (13)		60	
CH ₃ OH 7 ₋₂ → 6 ₋₂ -E	78.5 ^h	4.30 (0.12)	355 (13)		60	
CH ₃ OH 7 ₋₂₋ → 6 ₋₂₋ -A	<50		60	^a
G11-NH ₃						
o-H ₂ O 1 ₁₀ → 1 ₀₁	31.2 (0.1)	4.9 (0.1)	-1.17 (0.03)	35 (0.3)	4	abs
o-H ₂ O 1 ₁₀ → 1 ₀₁	33.2 (0.1)	0.8 (0.1)	>-3.30	35 (0.3)	4	abs
o-H ₂ O 1 ₁₀ → 1 ₀₁	37.1 (0.1)	1.5 (0.1)	-1.00 (0.04)	35 (0.3)	4	abs ^f
o-H ₂ ¹⁸ O 1 ₁₀ → 1 ₀₁	29.9 (0.2)	2.2 (0.4)	-0.51 (0.1)	31 (0.3)	8	abs
N ₂ H ⁺ 6 → 5	31.0 (0.2)	3.4 (0.4)	18 (2)		4	
N ₂ H ⁺ 3 → 2	30.7 (0.1)	2.3 (0.1)	1080 (40)		100	22.3'' ^g
C ¹⁷ O 3 → 2	30.7 (0.6)	5.1 (1.5)	120 (30)		60	
C ³⁴ S 7 → 6		60	^a
CH ₃ OH (all lines)		60	^a
G11-MM						
o-H ₂ O 1 ₁₀ → 1 ₀₁	27.8 (2.0)	9.1 (2.3)	43 (2)			
o-H ₂ O 1 ₁₀ → 1 ₀₁	28.7 (0.2)	23.0 (1.3)	24 (4)			
o-H ₂ O 1 ₁₀ → 1 ₀₁	30.9 (0.1)	4.4 (0.1)	>-3.16	44 (0.7)	5	abs
o-H ₂ O 1 ₁₀ → 1 ₀₁	37.5 (0.1)	1.2 (0.1)	-1.08 (0.05)	44 (0.7)	5	abs ^f
o-H ₂ ¹⁸ O 1 ₁₀ → 1 ₀₁	< -0.03	40 (0.7)	8	abs ^a
N ₂ H ⁺ 6 → 5	29.6 (0.1)	2.7 (0.1)	84 (2)		5	
N ₂ H ⁺ 3 → 2	29.6 (0.1)	5.0 (0.1)	1800 (43)		180	0.0'' ^g
C ¹⁷ O 3 → 2	29.6 (0.2)	3.0 (0.3)	570 (50)		75	
C ³⁴ S 7 → 6	29.2 (0.3)	6.3 (0.7)	160 (10)		75	
CCH 4 ₅₅ → 3 ₄₄	29.2 ^c	4.4 (0.2)	190 (10)		75	
CCH 4 ₄₄ → 3 ₃₃	29.2 ^c	4.0 (0.2)	190 (10)		75	
CH ₃ OH 7 ₋₁ → 6 ₋₁ -E	29.44 (0.04)	5.0 (0.1)	317 (5)		75	
CH ₃ OH 7 ₀ → 6 ₀ -E	29.37 (0.13)	2.1 (0.3)	96 (11)		75	
CH ₃ OH 7 ₁ → 6 ₁ -E	29.78 (0.09)	3.2 (0.2)	118 (7)		75	
CH ₃ OH 7 ₀₊ → 6 ₀₊ -A	29.9 (0.1)	4.1 (0.2)	289 (11)		75	

Notes. ^(a) Non-detection. ^(b) Marginal detection. ^(c) Possible blend, systemic velocity assumed. ^(d) Negatives indicate optical depth of absorption. ^(e) 1 σ rms. ^(f) Foreground. ^(g) Pointing offset between N₂H⁺ APEX observations and HIFI ^(h) Lines blended. systemic velocity assumed and lines fit simultaneously. Uncertainties listed are the formal 1 σ errors on the Gaussian fit. Lower limits identified by >, upper limits by <.

Table 5: Classification of line widths

Clump	Narrow ($< 3 \text{ km s}^{-1}$)	Intermediate (3 to 7 km s^{-1})	Broad ($> 7 \text{ km s}^{-1}$)
G28-NH ₃	H ₂ ¹⁸ O, N ₂ H ⁺	H ₂ O, C ¹⁷ O	H ₂ O _e
G28-MM	H ₂ O, H ₂ ¹⁸ O, C ¹⁷ O	H ₂ O, N ₂ H ⁺ , CH ₃ OH, C ³⁴ S, CCH	H ₂ O _e , CH ₃ OH
G11-NH ₃	H ₂ O, H ₂ ¹⁸ O, N ₂ H ⁺	H ₂ O, C ¹⁷ O	
G11-MM	H ₂ O, N ₂ H ⁺ , C ¹⁷ O	H ₂ O, CH ₃ OH, C ³⁴ S, CCH	H ₂ O _e

Notes. H₂O and H₂¹⁸O refer to widths of absorption lines. H₂O_e refers to the emission lines.

Table 6: Emission line column densities

Line	Velocity (km s^{-1})	Δv (km s^{-1})	T_{mb} (mK)	N_5 (10^{14} cm^{-2})	N_6 (10^{14} cm^{-2})	N_7 (10^{14} cm^{-2})
G28-NH ₃ $T_{kin} = 13.2 \text{ K}$						
N ₂ H ⁺ 6 → 5	79.7 (0.3)	2.9 (0.7)	11 (2)	2.2	0.2	0.02
C ¹⁷ O 3 → 2	79.3 (0.8)	5.2 (1.9)	110 (40)	5.3	4.8	4.8
G28-MM $T_{kin} = 16.0 \text{ K}$						
N ₂ H ⁺ 6 → 5	78.3 (0.1)	3.8 (0.1)	404 (2)	27.2	2.3	0.37
C ¹⁷ O 3 → 2	78.2 (0.1)	2.9 (0.1)	1800 (40)	40.6	37.6	37.0
C ³⁴ S 7 → 6	77.6 (0.1)	5.6 (0.2)	260 (10)	34.8	3.0	0.38
G11-NH ₃ $T_{kin} = 12.7 \text{ K}$						
N ₂ H ⁺ 6 → 5	30.9 (0.1)	2.7 (0.3)	19 (2)	4.3	0.4	0.05
C ¹⁷ O 3 → 2	30.7 (0.6)	5.1 (1.5)	120 (30)	6.0	5.5	5.4
G11-MM $T_{kin} = 13.8 \text{ K}$						
N ₂ H ⁺ 6 → 5	29.6 (0.1)	2.7 (0.1)	85 (2)	9.1	0.92	0.13
C ¹⁷ O 3 → 2	29.6 (0.2)	3.0 (0.3)	570 (50)	15.0	14.0	13.8
C ³⁴ S 7 → 6	29.2 (0.3)	6.3 (0.7)	160 (10)	43.0	3.8	0.46

Notes. N_5 is the calculated column density assuming a gas number density of 10^5 cm^{-3} , likewise for N_6 and N_7

Table 8: o-H₂O Column density from absorption lines

ID	v (km s^{-1})	Δv (km s^{-1})	τ	$N(\text{o-H}_2\text{O})$ (10^{14} cm^{-2})	χ (10^{-8})
G28-NH ₃	81.4	3.3	$> 4.5^a$	> 0.72	...
	79.4 ^c	1.2	0.76	21.6	3.7
G28-MM	79.3	6.6	$> 3.8^a$	> 1.2	...
	82.8	1.5	2.2^a	0.16	...
	78.3 ^c	1.1	0.4	10.8	0.33
G11-NH ₃	31.2	4.9	1.7	0.28	...
	33.2	0.76	$> 3.3^a$	> 0.12	...
	29.9 ^c	2.2	0.5	26.1	3.1
G11-MM	30.9	4.4	$> 3.2^a$	> 0.69	...
	30.0 ^b	2.0	< 0.03	< 1.5	0.07 – 0.15

Notes. ^(a) Lower limit, since line is very close to saturated ^(b) Estimated upper limit based on non detection of H₂¹⁸O feature assuming an abundance with respect to H₂O of 500 and adopting a line width of 2.0 km s^{-1} . ^(c) Measured H₂¹⁸O and abundance with respect to H₂O of 500

Table 10: Mass infall rates

Clump	V_{infall} (km s^{-1})	R (pc)	\dot{M}_5^a ($M_\odot \text{ yr}^{-1}$)	\dot{M}_6 ($M_\odot \text{ yr}^{-1}$)	\dot{M}_7 ($M_\odot \text{ yr}^{-1}$)
G28-NH ₃	1.2	0.05 ¹	2.1e-04	2.1e-03	2.1e-02
G28-MM	0.8	0.1 ¹	5.7e-04	5.7e-03	5.7e-02
G11-NH ₃	0.8	0.04 ^b	9.2e-05	9.2e-04	9.2e-03
G11-MM	1.7	0.04 ²	1.9e-04	1.9e-03	1.9e-02

Notes. ^(a) Infall rate for velocity of broadest absorption component assuming densities of 10^5 cm^{-3} , 10^6 cm^{-3} and 10^7 cm^{-3} ^(b) Core size assumed to be the same G11-MM. References. (1) Chen et al. (2010); (2) Gómez et al. (2011)

Table 11: Dynamic structures within IRDC clumps

Component	Properties	Tracer
Quiescent envelope	$\Delta V < 3 \text{ km s}^{-1}$ at systemic V	H ₂ ¹⁸ O, N ₂ H ⁺ , NH ₃ ^a , C ¹⁷ O ^b
Envelope	ΔV from 3 to 7 km s^{-1} at systemic V	CH ₃ OH, C ³⁴ S, CCH, C ¹⁷ O ^b
Infall	ΔV from 3 to 7 km s^{-1} redshifted V	H ₂ O absorption
Outflow	$\Delta V > 7 \text{ km s}^{-1}$ at systemic velocity	H ₂ O emission

Notes. ^(a) From Pillai et al. (2006a). ^(b) C¹⁷O is broader than 3 km s^{-1} for the NH₃ positions.